Rock Mechanics Bulletin 3 (2024) 100115

Contents lists available at ScienceDirect

Rock Mechanics Bulletin

journal homepage: www.keaipublishing.com/en/journals/rock-mechanics-bulletin

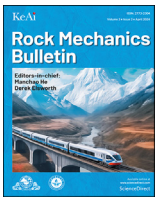

Full Length Article

Modelling the brittle rock failure by the quaternion-based bonded-particle model in DEM

Tao Zhao *, Philip E.F. Collins

Department of Civil and Environmental Engineering, Brunel University London, London, UB8 3PH, United Kingdom

ARTICLE INFO

Keywords:
Brittle failure
Quaternion
DEM bonded model
Uniaxial compression test
Rate dependent
Internal damage

ABSTRACT

This paper presents an investigation of brittle rock failure by the quaternion-based bonded-particle model in discrete element method (DEM). Unlike traditional approaches that utilize Euler angles or rotation matrices, this model employs unit quaternions to represent the spatial rotations of particles. This method simplifies the representation of 3D rotations, providing a more intuitive framework for modelling complex interactions in granular materials. The numerical model was validated by the uniaxial compression tests on rock, with good agreement with well-documented experimental data in terms of the rock uniaxial compression strength (UCS) and failure mode. During loading, the rock sample demonstrated a linear-elastic response at an axial strain of smaller than 0.45%. However, as internal bond breakage accumulated, this linear relationship weakened, and the stress-strain curve began to deviate from its initial linear trajectory. The bond breakage and the overall deformation of the rock were primarily controlled by the shear bonding force. The UCS was achieved at an axial strain of 0.625%, at which point the internal shear bonding force chains were predominantly aligned vertically. The brittle failure occurred when the internal damage of solids nucleated to form an interconnected failure plane, accompanied by a sharp rise in the internal damage ratio. The area of failure plane increased with the loading strain rate, gradually transforming the failure pattern from the local damage to a complete fragmentation.

1. Introduction

Brittle failure in rock masses is a critical phenomenon in geotechnical engineering and earth sciences (Carlà et al., 2017; Keneti and Sainsbury, 2018; Zou and Li, 2021; Xu et al., 2023). It refers to the abrupt and often unforeseeable fracturing of rock under stress levels exceeding its ultimate strength. This failure pattern is typically characterized by a rapid propagation of internal damage without significant plastic deformation (Hajiabdolmajid et al., 2002). It can pose significant risks, especially in the context of construction, mining, and natural disasters (Xu et al., 2006; Barton and Shen, 2017). Events such as landslides, rockfalls, and mine collapses, which are direct consequences of brittle rock failure, can have devastating impacts, endangering human lives and inflicting severe property damage (Sun et al., 2023). In natural settings, brittle rock failure can also contribute to seismic processes, notably in fault zones (Ohnaka, 2013; Lv et al., 2022). Therefore, understanding the mechanics of brittle rock failure is essential for predicting and mitigating these hazards.

Research in this area typically involves a combination of experimental, analytical, and computational approaches (Wang and Cai, 2018). Laboratory experiments, such as uniaxial and triaxial compression tests, are conducted to understand the failure characteristics under controlled conditions (Ma et al., 2023; Malachi Ozoji et al., 2024). For computational methods, the discrete element method (DEM) has been widely used to analyze the brittle failure of solid materials, e.g. rock fragmentation (Potyondy and Cundall, 2004; Duan and Kwok, 2016; Shen et al., 2017; Xu et al., 2020), particle crushing (de Bono et al., 2015; Shen et al., 2016; Manso et al., 2018) and damage of cemented geomaterials (Thornton et al., 1999; Nova et al., 2003; Rait et al., 2012), due to its ability to model the complex brittle responses of solid mass under external loading, such as crack initiation and propagation (Alassi and Holt, 2012; Zhao and Crosta, 2018). At failure, the internal solid damage propagates and nucleates quickly within the solid mass due to the breakage of inter-particle cementations (i.e. bonds). It can be induced by excessive compressive, tensile or shear loading, together with the transmission and reflection of stress waves at impact (Thornton et al., 1999; Crosta et al., 2007). The characteristics and energy dissipation mechanisms of solid fragmentation (e.g. fracturing stress, size and number of fragments) depend primarily on the material shear strength and loading strain rate (Grady, 1981).

In numerical analyses of solid fragmentation by DEM, the complex

* Corresponding author.
E-mail address: tao.zhao@brunel.ac.uk (T. Zhao).

https://doi.org/10.1016/j.rockmb.2024.100115
Received 31 January 2024; Received in revised form 5 March 2024; Accepted 6 March 2024
Available online 6 March 2024

three-dimensional particle spatial rotations should be considered in detail, so that the stretching, bending and twisting deformations of inter-particle bonds can be evaluated correctly (Wang, 2009). Attempts to represent rotations of a rigid body by Euler angles have been proved complicated and suffer from the gimbal lock problem (i.e. inherent singularity) (Wang, 2009; Seelen et al., 2016). Alternatively, the incremental displacement method and rotation matrices have been widely used in DEM to compute particle interaction forces in a 3D space (Jiang et al., 2005; Modenese, 2013). However, this approach involves complicated vector manipulations and it is only valid when the relative displacement between two particles is extremely small during each integration step. To overcome these problems, the unit quaternions, a generalization of complex numbers in mathematics, have been employed to represent the rotations of rigid objects in a 3D space (Obermayr et al., 2013), from which the interaction forces and moments can be conveniently and accurately determined. In this approach, the breakage criterion of the inter-particle bond is described as a combined contribution of normal and shear bonding forces, and the rolling and twisting moments (Shen et al., 2016; Zhao et al., 2018).

The quaternion was first proposed by Hamilton (1844) as a number system that extends the complex numbers. It can be used to represent the spatial rotation of a rigid object in a concise and elegant form (Wang et al., 2013). The quaternions have been widely applied in various research fields, such as computer graphics (Ling et al., 2022), robotics (Graells Rovira and Mirats Tur, 2009), aerospace (Zhang et al., 2015) and molecular dynamics (Walmsley, 1988). In this study, a quaternion-based bonded-particle DEM model was employed to analyze the brittle failure of solids following the pioneering work by Wang (2009). Specifically, the unit quaternions were used to represent rigid particle rotations in a 3D space and calculate the relative displacements between the two bonded particles at a specified time. Then, the particle interactions, e.g. normal and shear bonding forces, bending and twisting moments, can be evaluated accordingly. In the calculation, multiple transformations of particle properties (e.g. position and contact forces) between the local and global coordinate frames by quaternion algebra are needed. This approach can effectively capture the complex interactions of a granular system involved in spatial rotations in a more realistic and reliable way. By modelling the uniaxial compression of solids with this model, the nature of brittle failure can be thoroughly understood. With proper calibrations, the proposed numerical model can significantly extend the applicability of DEM modelling in solid mechanics.

2. Methodology

The DEM is an effective technique for analyzing the mechanical behavior of granular materials, and it can also be used to simulate the brittle failure of rock masses. This approach decomposes a material system into numerous individual particles, each considered as a separate entity. The interactions among these particles, including collisions, friction, and bonding, are simulated through a set of established physical and empirical principles. According to Newton's second law of motion, the equations governing the translational and rotational motions of a single particle i can be expressed as,

$$m_i \frac{d^2}{dt^2} x_i = m_i g + \sum (\boldsymbol{F}_{i,c} + \boldsymbol{F}_{i,b}) \tag{1}$$

$$I_i \frac{d}{dt} \boldsymbol{\omega}_i = \sum_c \boldsymbol{M}_i \tag{2}$$

where m_i is the mass of particle i; x_i is the position of its centroid; $\boldsymbol{g}$ is the gravitational acceleration; $\boldsymbol{F}_{i,c}$ and $\boldsymbol{F}_{i,b}$ are the inter–particle contact and bonding forces exerted by the neighboring particles on particle i. The summation of the inter–particle interaction forces is over all contacts and bonds with particle i; I_i is the moment of inertia about the particle centroid; $\boldsymbol{\omega}_i$ is the angular velocity; $\boldsymbol{M}_i$ is the moment acting on particle i, including moments induced by the tangential contact and bonding forces, bending and twisting moments between bonded particles.

The contact forces and moments between any two particles in contact can be calculated by well-defined constitutive models, e.g. linear elastic spring-dashpot model or Hertz-Mindlin model (Modenese, 2013; Utili et al., 2015). Here, the governing equations of a linear spring-dashpot model are expressed as follows,

$$\vec{\boldsymbol{F}}_{\boldsymbol{n}} = k_n \cdot u_n - \beta \Delta v \tag{3}$$

$$\vec{\boldsymbol{F}}_s^{\,i} = \begin{cases} \vec{\boldsymbol{F}}_s^{\,i-1} + k_s \cdot \Delta u_s, \text{if } \left|\vec{\boldsymbol{F}}_s^{\,i-1}\right| < \mu \left|\vec{\boldsymbol{F}}_{\boldsymbol{n}}\right| \\ \mu \left|\vec{\boldsymbol{F}}_{\boldsymbol{n}}\right|, \text{if } \left|\vec{\boldsymbol{F}}_s^{\,i-1}\right| \geq \mu \left|\vec{\boldsymbol{F}}_{\boldsymbol{n}}\right| \end{cases} \tag{4}$$

$$\vec{\boldsymbol{M}} = \vec{\boldsymbol{F}}_s^{\,i} \times \vec{\boldsymbol{r}} \tag{5}$$

where $\boldsymbol{F_n}$, k_n, u_n and Δv are the normal contact force, stiffness, overlapping distance and relative velocity between two particles in contact; β is the damping coefficient; $\boldsymbol{F}_s^i$ and $\boldsymbol{F}_s^{i-1}$ are the shear forces calculated at the current and previous iteration time steps, respectively; k_s and Δu_s are the shear stiffness and incremental shear displacement; $\boldsymbol{M}$ is the shear induced moment; $\boldsymbol{r}$ is the vector linking the particle center and contact point. In this study, the viscous damping force (i.e. proportional to the relative velocity between two particles in contact, Δv) has been employed in the normal direction of particle contact to replicate the energy dissipation by shearing off particle asperities and plastic deformations of the contacts.

The inter-particle bonding forces are calculated according to the relative translational and rotational displacements between the two bonded particles (Wang, 2009), which requires a sophisticated method to evaluate the translational and rotational motions of individual particles in a 3D space. For any two bonded spherical particles (i.e. particle 1 and 2), in a global space-fixed frame, the initial positions of particle centers at time T = 0 are defined as $\overrightarrow{r_{10}} = x_{10}\boldsymbol{i} + y_{10}\boldsymbol{j} + z_{10}\boldsymbol{k}$ and $\overrightarrow{r_{20}} = x_{20}\boldsymbol{i} + y_{20}\boldsymbol{j} + z_{20}\boldsymbol{k}$, with $\boldsymbol{i}$, $\boldsymbol{j}$, $\boldsymbol{k}$ are unit vectors that define the direction along the x, y, and z-axes, respectively. Their orientations can be represented by unit quaternions $\boldsymbol{p}$ and $\boldsymbol{q}$, respectively, with the initial values as $\langle 1, (0,0,0) \rangle$. $\boldsymbol{p}$ and $\boldsymbol{q}$ are dynamically updated through quaternion integration as the simulation progresses. For detailed information on this process, refer to Appendix A. The initial distance vector ($\overrightarrow{r_0}$) between the two particles is,

$$\overrightarrow{r_0} = \overrightarrow{r_{20}} - \overrightarrow{r_{10}} \tag{6}$$

At T = t, the distance vector becomes $\overrightarrow{r_b}$ in the local coordinate system.

The calculation of interaction forces requires the evaluation of relative particle displacement components in the normal, shear, bending and twisting directions during the time interval from $T = 0$ to t. The stiffness of bonding force components in the normal, shear, bending and twisting directions are defined as k_{bn}, k_{bs}, k_b and k_t, respectively, and can be computed according to the particle radius, Young's modulus (E_b) and Poisson ratio (υ) of a particle bond (see Zhao et al. (2017)). The following algorithm will illustrate the calculation of particle interaction forces through the decomposition of relative particle displacements into the translational and rotational components in the local coordinate system $O_1 - X_1Y_1Z_1$.

The normal bonding force acting on particle 1 in $O_1 - X_1Y_1Z_1$ is expressed as,

$$\overrightarrow{\boldsymbol{F}_{\boldsymbol{bnt}}} = k_{bn} \times (|\overrightarrow{r_b}| - |\overrightarrow{r_0}|) \times \overrightarrow{r_b} / |\overrightarrow{r_b}| \tag{7}$$

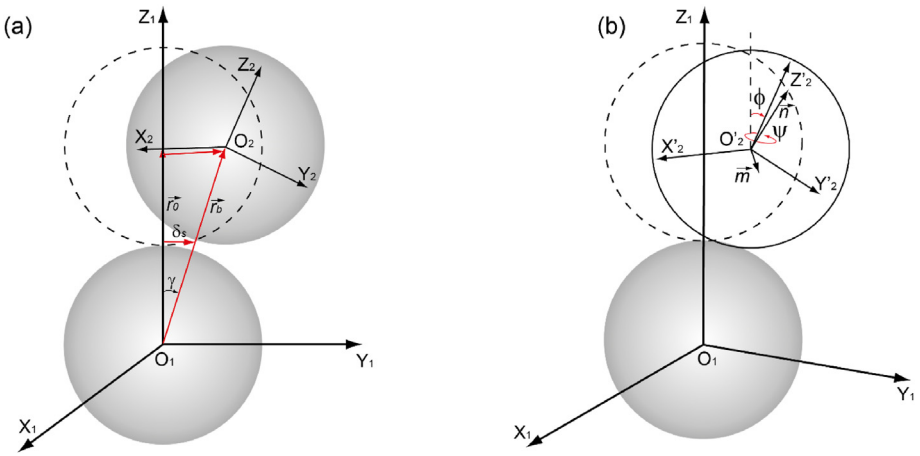

Fig. 1. (a) Translational displacement of particle 2 relative to particle 1; (b) Rotational displacement of particle 2 relative to particle 1 in the local body-fixed coordinate frame $O_1 - X_1Y_1Z_1$. The dashed circle represents the initial position of particle 2 at T = 0. The position of particle 2 relative to particle 1 is represented by the vectors $\vec{r_0}$ and $\vec{r_f}$ in $O - XYZ$, while it is $\vec{r_b}$ in $O_1 - X_1Y_1Z_1$ at T = t.

To calculate the shear bonding force, the shear displacement (δ_s) is first computed at the contact point between the two particles (see Fig. 1 (a)), as,

$$\delta_s = \frac{1}{2} \times |\vec{r_0}| \times \cos^{-1}(\vec{r_b} \cdot \vec{r_0} / (|\vec{r_b}||\vec{r_0}|)) \tag{8}$$

Here, the shear displacement is assumed to be very small during the time interval T = 0 to t. Then, the shear bonding force can be computed as,

$$\overrightarrow{F_{bst}} = k_{bs} \times \delta_s \times \vec{n_s} \tag{9}$$

where the orientation of shear force is computed as $\vec{n_s} = \vec{r_b} \times (\vec{r_b} \times \vec{r_0}) / |\vec{r_b}||\vec{r_b} \times \vec{r_0}|$,

The shear force induced moment is then computed as,

$$\overrightarrow{M_{st}} = 0.5 \times \overrightarrow{F_{bst}} \times \vec{r_b} \tag{10}$$

According to Wang (2009), the rotational displacement of Particle 2 relative to Particle 1 can be decomposed into twisting and bending components, which are sequence-independent. Fig. 1(b) depicts Particle 2 bending around the unit orientation vector $\vec{m}$ relative to Particle 1, followed by a twisting motion around another unit orientation vector $\vec{n}$. In the local coordinate system $O_1 - X_1Y_1Z_1$, the bending (φ) and twisting (ψ) angles can be evaluated using to the algorithm outlined in Wang (2009).

The bending moment can be computed as,

$$\overrightarrow{M_{br}} = k_b \times \varphi \times \vec{m} \tag{11}$$

The bending induced shear force and moment can be calculated as:

$$\overrightarrow{F_{bsr}} = 0.5 \times k_{bs} \times \varphi \times |\vec{r_0}| \times \overrightarrow{n_{sp}} \tag{12}$$

$$\overrightarrow{M_{sr}} = -0.5 \times \overrightarrow{F_{bsr}} \times |\vec{r_0}| \times \vec{m} \tag{13}$$

where $\overrightarrow{n_{sp}} = (0, 0, 1) \times \vec{m}$ is the orientation of shear force.

Thus, the twisting moment can be computed as,

$$\overrightarrow{M_{tr}} = k_t \times \psi \times \vec{n} \tag{14}$$

Finally, all the forces and moments acting on Particle 1 should be transposed back to the global space-fixed frame $O - XYZ$. This is achieved by conjugation of these vectors with Particle 1's orientation quaternion $\boldsymbol{p}$ (see Appendix A for an in-depth theoretical explanation) as,

$$\begin{aligned} \overrightarrow{F_{bn}} &= \boldsymbol{p}\overrightarrow{F_{bnt}}\boldsymbol{p}^{-1} \\ \overrightarrow{F_{bs}} &= \boldsymbol{p}\left(\overrightarrow{F_{bst}} + \overrightarrow{F_{bsr}}\right)\boldsymbol{p}^{-1} \\ \overrightarrow{M_s} &= \boldsymbol{p}\left(\overrightarrow{M_{st}} + \overrightarrow{M_{sr}}\right)\boldsymbol{p}^{-1} \\ \overrightarrow{M_b} &= \boldsymbol{p}\overrightarrow{M_{br}}\boldsymbol{p}^{-1} \\ \overrightarrow{M_t} &= \boldsymbol{p}\overrightarrow{M_{tr}}\boldsymbol{p}^{-1} \end{aligned} \tag{15}$$

Here, it is assumed that the two spherical particles have the same radius. For particles of different radii, $\overrightarrow{M_{st}}$ and $\overrightarrow{M_{sr}}$ should be scaled proportionally to the radius of each particle.

The criterion for bond breakage is expressed as,

$$\frac{|\overrightarrow{F_{bn}}|}{F_{bnMax}} + \frac{|\overrightarrow{F_{bs}}|}{F_{bsMax}} + \frac{|\overrightarrow{M_b}|}{M_{bMax}} + \frac{|\overrightarrow{M_t}|}{M_{tMax}} \geq 1 \tag{16}$$

where F_{bnbMax}, F_{bsMax}, M_{bMax} and M_{tMax} are the normal, shear, bending and twisting bonding strengths of a specific bond, respectively. Their values can be determined by the cohesion of bond (c) (see (Zhao et al., 2017)).

3. Numerical model validations

In this study, the well-developed open-source DEM code ESyS-Particle (Weatherley et al., 2021) has been employed to explore the phenomena of brittle failure in solids during uniaxial compression experiments. This code incorporates comprehensive algorithms for a quaternion-based particle bonding model, as detailed in Section 2.

3.1. Model configuration

The DEM model is employed to simulate the standard uniaxial compression test on a cubic rock sample, which is assumed to be completely dry. The uniaxial compression test has been widely used to evaluate the uniaxial compression strength (UCS) of rock mass in laboratory (Yesiloglu-Gultekin et al., 2013). During the test, a model rock sample is generated by packing a dense assembly of spherical particles with radii ranging from 0.75 to 1.5 mm in a cube of dimensions 50 mm × 50 mm × 100 mm (see the inset plot in Fig. 2). These particles are bonded together by the quaternion-based bonded-particle model. Notably, the DEM model exhibits a high void ratio, mirroring the characteristics of highly porous materials such as sandstones. Then, the sample is compressed by vertical loading plates at both ends under a constant loading strain rate. The strain rate is defined as the ratio of the velocity at which the loading plate moves to the height of the sample. The loading strain rate ($\dot{\varepsilon}$) ranges from 0.05 s^{-1} to 10 s^{-1} for a series of tests, so that its

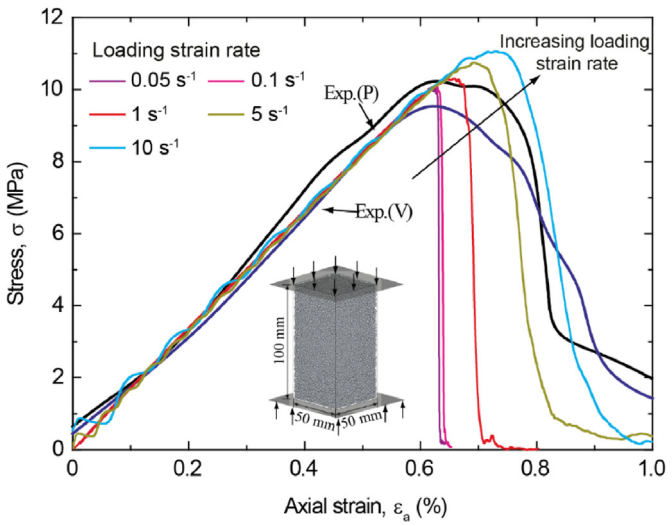

Fig. 2. The stress-strain relationship of uniaxial compression test on solid samples. The DEM model configuration is shown in the inset plot. The compression of constant loading strain rate is applied on loading plates at both ends of the sample. "Exp.(P)" and "Exp.(N)" stand for experimental data of uniaxial compression test on coal rock with parallel and normal beddings to the loading direction, respectively (the strain rate is 0.01 s^{-1}).

influence on the micro- and macro-responses of solids can be analyzed. The input parameters of the simulations were selected by trial and error (see Table 1), to ensure that the shear strength and stiffness of the solid specimen can match the available experimental data of uniaxial compression tests on coal rock samples as reported in Liu et al. (2015).

3.2. Results

Fig. 2 illustrates the stress-strain relationships of rock responses during the uniaxial compression tests in DEM and the comparison with the experimental data on coal rock samples by Liu et al. (2015). In the cited experimental data, the effect of stratigraphic layer orientation in coal rock was assessed using specimens oriented both parallel and perpendicular to the horizontal plane. These orientations are denoted in Fig. 2 as Exp. (P) for parallel bedding and Exp. (V) for vertical bedding, respectively. According to the figure, the numerical results can match well the experimental data for the strain rate smaller than 0.1 s^{-1} with respect of the bulk Young's modulus (E) and the uniaxial compression strength (UCS). At relatively large loading strain rate (e.g. $\geq$ 1 s^{-1}), E remained approximately constant, while UCS increased quickly with the loading strain rate, showing a strong rate dependent behavior. Additionally, when the strain rate exceeded 5 s^{-1}, the stress-strain curve displayed noticeable oscillations during the initial loading phase. This is attributed to the frequent transmission and reflection of stress waves at both ends of the loading plates, coupled with the high inertia associated with solid deformation. These oscillations intensified in tests with very high loading strain rates (for instance, 10 s^{-1}), characterized by larger magnitudes and longer periods. However, as the loading stress nears the peak values (i.e. UCS), these oscillations gradually diminished. This reduction occurred as the formation of strong force chains starts to predominate within the solid sample (Zhao and Crosta, 2018). The numerical results demonstrate that stress oscillation is a consistent feature across all tests, and it is heavily influenced by the loading strain rate. This particular aspect of solid response, especially in the context of dynamic tests on rock, has been thoroughly examined and discussed in detail in the literature Zhang and Zhao (2014). To minimize this effect, adopting a quasi-static loading condition with a very low strain rate is advisable. This approach can significantly reduce the magnitude and period of stress oscillation, leading to negligibly small values and resulting in smoother stress-strain curves.

Table 1
Input parameters of the DEM model for the uniaxial compression tests.

DEM Parameters	Value	DEM Parameters	Value
Particle radius, r (mm)	[0.75, 1.5]	DEM time step, Δt (s)	10^{-7}
No. of particles, N	31,361	Packing porosity, n	0.48
Density, ρ (kg/m^3)	2650	Young's modulus of particle, E (GPa)	8.2
Particle friction angle, φ(°)	30	Young's modulus of bond, E_b (GPa)	2
Particle Poisson ratio, υ	0.25	Cohesion of bond, c (MPa)	20.6
Gravitational acceleration, g (m/s^2)	0.0	Viscous damping coefficient, β	0.01

To investigate the rate dependent behavior, the relationship between the uniaxial compression strength of the bonded solid mass and loading strain rate ($\dot{\varepsilon}$) is presented in Fig. 3. According to the figure, the UCS exhibited a gradual increase with the loading strain rate when $\dot{\varepsilon}$ was smaller than 1. However, there was a sharp increase in UCS when $\dot{\varepsilon}$ became greater than or equal to 1. This trend appears to follow an exponential relationship, aligning closely with the findings reported in references Zhao et al. (2017) and Zhang and Zhao (2014). These studies indicate that the strength of solids can significantly increase under dynamic loading conditions, particularly at high loading strain rates typical of impact scenarios. The fitting curve of the DEM results in this study is,

$$UCS = -1.09e^{-0.2\dot{\varepsilon}} + 11.18 \quad (R^2 = 0.986) \tag{17}$$

The corresponding distribution of internal rock damages at the failure state can also be visualized for different tests, as shown in Fig. 4. In the analyses, once a bond breaks, two red spheres are plotted at the centers of particles linked by that bond, with the diameter proportional to the ratio of broken bonds relative to each particle. This is especially relevant in scenarios where a single particle is concurrently bonded with multiple other particles. At the failure state, the internal damage nucleated to form an interconnect plane (i.e. failure plane), such that the solid sample broke into several major fragments. The failure plane was relatively small and located at the upper edge of the sample for tests of low loading strain rate (e.g. 0.05 s^{-1}, 0.1 s^{-1}), exhibiting a sudden brittle failure mode (see also the sudden drop of stress in Fig. 2). This mode of rock failure could pose significant risks due to the minimal damage information that can be obtained from surface deformations of the sample. As the strain rate of the load increased, the internal damage progressively spread to the lower regions, encompassing a considerably extensive area. This results in a

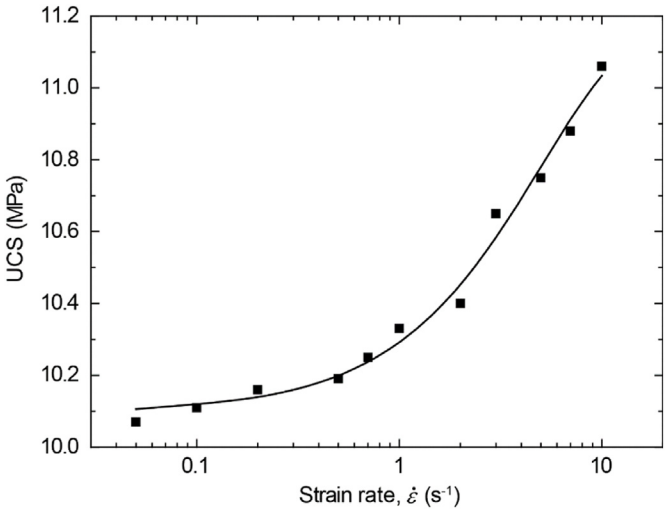

Fig. 3. The uniaxial compression strength (UCS) of rock samples tested under different loading strain rates.

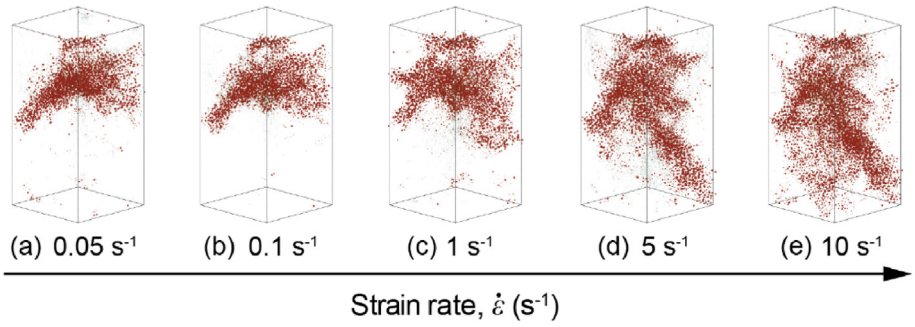

Fig. 4. Distribution of internal rock damages for tests under different loading strain rate presented as red dots. (For interpretation of the references to color in this figure legend, the reader is referred to the Web version of this article.)

thorough fragmentation of the solid structure, indicating severe internal rock damages.

Fig. 5 illustrates the evolution of uniaxial compression stress (σ) and internal rock damage ratio (D) with the axial strain (ε_a) for a test at loading strain rate of 0.1 s^{-1}. Here, the internal damage ratio (D) is defined as the percentage of broken bonds occurring during the uniaxial compression test over the initial number of bonds in the intact rock mass before the test. In addition, the bonding force chains are also plotted in Fig. 6 as a network of straight lines connecting the particle centers, with the thickness proportional to the magnitude of particle bonding force. On the plot, the normal and shear bonding force chains are colored black and green, respectively. According to the figure, prior to any internal bond breakage ($\varepsilon_a < \varepsilon_{a0} = 0.45\%$), the loading stress increased linearly with the strain, exhibiting a linear-elastic response of solids under compression. As compression progressed, further bond breakages occurred and the material's linear elasticity was weakened, causing the stress-strain curve to deviate from its initial linear trajectory. As σ gradually approached the peak value at ε_a = 0.51%~0.625%, the rate of stress increase slowed down and the internal bonding force chains became predominantly aligned in a vertical orientation (see green lines Fig. 6 (a), ε_a = 0.625%). After reaching UCS of 10.1 MPa at ε_a = 0.625%, σ decreased slightly due to the accumulation of internal rock damages. After $\varepsilon_a = 0.63\%$, D started to increase sharply, and the internal damage of solids nucleated to form an interconnected failure plane (see Fig. 6 (b, c)). This process led to a sudden drop of σ from the peak to the minimum value of 0.03 MPa, showing apparent brittle failure response of solids. D reached a relatively stable value of 10% at $\varepsilon_a = 0.64\%$ when the detached solid fragments had quite few contacts with each other. At this stage, the internal bonding force chains became negligibly small and the distribution of internal damage remained stable (see Fig. 6 (d), ε_a = 0.64%). Further compression of the solid fragments could slightly increase the internal damages (see Fig. 6 (e), $\varepsilon_a = 0.645\%$), with little change of stress. The final stable value of D was 11.86%.

The spatial distribution of the final stable internal damage zone is depicted through 3D visualization from multiple angles in Fig. 7. The figure reveals that the internal failure plane intersected with the upper edge of the solid sample, inclining at an angle of approximately 60°. This failure mode is consistent with the principles defined in the Mohr-Coulomb failure criteria, and matches the experimental observation (Fig. 7(e)) presented in Liu et al. (2015). As a result of this failure, the solid sample fragmented into two distinct parts: a smaller, upper wedge-shaped block and a larger, solid block at the bottom.

During the simulation, the maximum force components at all contacts (i.e. the normal (F_{bn}) and shear (F_{bs}) bonding forces, the normal (F_n) and shear (F_s) contact forces) have been recorded. Fig. 8 illustrates the evolution of internal force components and damage ratio with the axial strain (ε_a) of the rock sample for test under the loading strain rate of 0.1 s^{-1}. Among all the force components, the shear bonding force (blue curve) was the largest, indicating that the brittle failure of solids was induced dominantly by shear deformations. The contact forces were negligibly small when compared to the bonding forces because the interactions between particles were mainly via bonds and few particles are in direct contact with each other before the intense fragmentations took place. Since the linear elastic constitutive models were employed, the

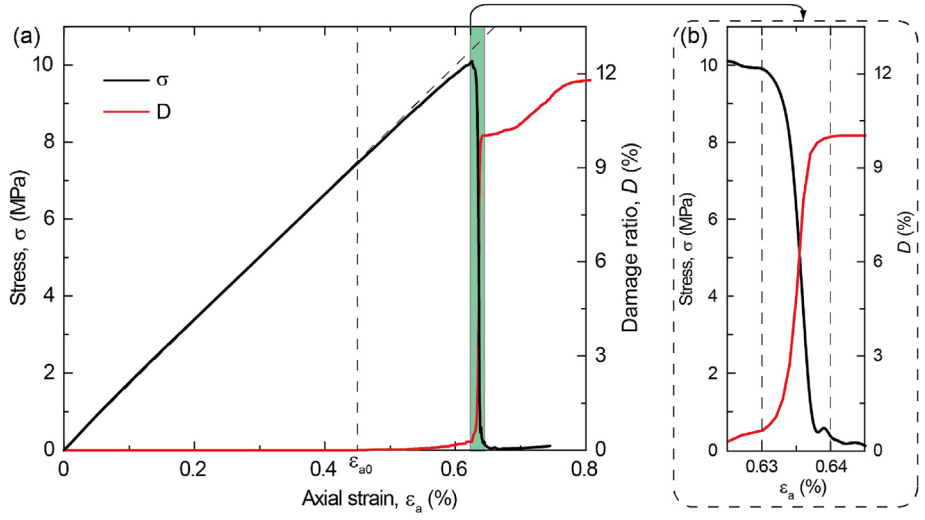

Fig. 5. Evolution of compressive loading stress (σ) and internal solid damage (D) with the axial strain for test of loading rate 0.1 s^{-1}. (a) The general evolution curves of σ and D; ε_{a0} = 0.45% marks the point at which the first internal bond breaks. (b) An enlarged view of the evolution curves for axial strain in the range of 0.615%–0.635%.

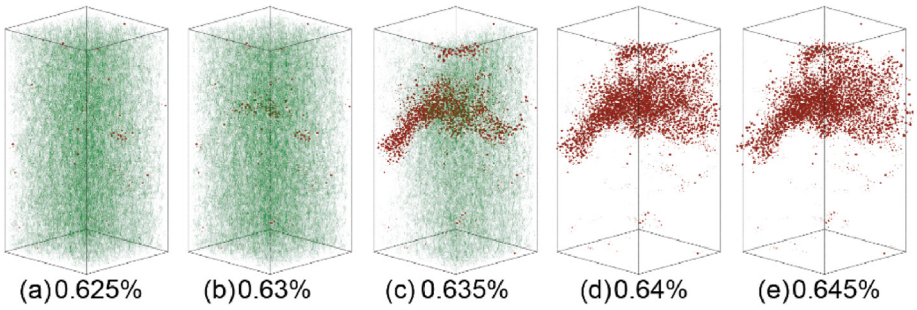

Fig. 6. The distribution of internal bonding force chains and solid damage (red dots) at different compression stages. (For interpretation of the references to color in this figure legend, the reader is referred to the Web version of this article.)

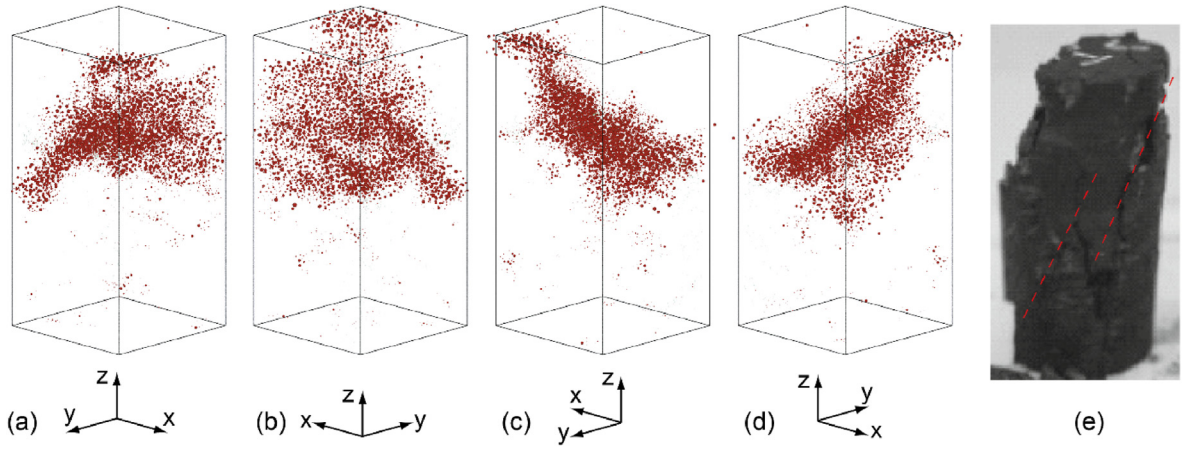

Fig. 7. Different views of the distribution of internal damage zone of the solids (red dots represent the internal damage zone). (a) front view; (b) back view; (c) left view; (d) right view. (e): the fractured coal rock sample after the uniaxial compression test (cited from Liu et al. (2015)). (For interpretation of the references to color in this figure legend, the reader is referred to the Web version of this article.)

force components all increased linearly with the axial strain, ε_a, at the initial compression stage before $\varepsilon_{a1} = 0.62$. As ε_a approached ε_{a1}, the rate of internal rock damage started to rise, and D increased apparently. For $\varepsilon_a > \varepsilon_{a1}$, the normalized maximum shear force exhibited a sudden increase to the peak value of 0.008, while F_{bn}, F_n and F_s correspondingly all showed slight increases. When F_{bs} was close the peak value, the whole solid mass cannot resist the external compressive loading and the internal solid damage started to nucleate quickly to form an interconnected failure plane (see Fig. 6 (b). The increasing rate of F_{bs} slowed down after $\varepsilon_a =$ 0.63% when the internal solid damage ratio started to rise rapidly (see Fig. 8 (b)). After reaching the peak value, F_{bs} dropped quickly as D increased. When D reached a relatively large and stable value of 10% at $\varepsilon_a = 0.64\%$, the decreasing rate of F_{bs} reduced gradually (see Fig. 8 (b)) due to the persistent particle contacts between detached fragments. The subsequent interactions between detached fragments leads to a slight increase of D and variations of F_{bn} and F_{bs}, while F_n and F_s remained negligibly small.

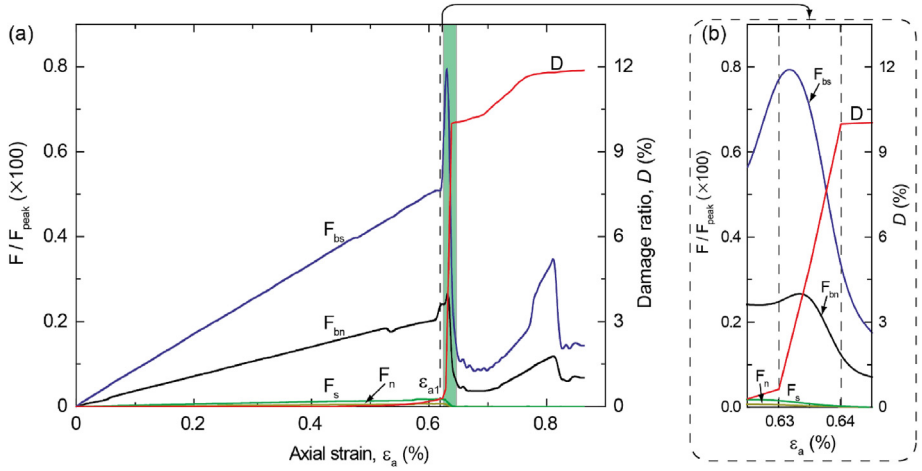

Fig. 8. Evolution of maximum particle interaction forces at contact and internal damage ratio (D) with the axial strain for test under loading strain rate of 0.1 s^{-1}. The force components are normalized by the peak force acting on the loading plates (F_{peak}). F_{bn}: normal bonding force; F_{bs}: shear bonding force; F_n: normal contact force; F_s: shear contact force. (a) The evolution curves of bonding and contact forces, and D; (b) An enlarged view of the evolution curves for axial strain in the range of 0.615%–0.635%.

4. Conclusions

In this study, the phenomenon of brittle failure in rock masses was explored using the Discrete Element Method (DEM), implemented through a quaternion-based bonded-particle model. The application of unit quaternions was chosen for its potential to more effectively handle the complex spatial rotations and interactions among bonded particles in 3D, as suggested by existing literature. The DEM model was calibrated from standard uniaxial compression tests on cubic rock samples by a good agreement in the stress-strain behavior and failure mode between the numerical and experimental testing results. The key research findings are summarized as follows.

(1) The numerical simulations of the uniaxial compression tests of rock sample revealed that the stress oscillation, uniaxial compression strength (UCS) and size of internal damage zone all increased with the loading strain rate, exhibiting strong rate-dependent mechanical behaviors. As the loading strain rate increased from 0.05 to 10 s^{-1}, the UCS increased from 10.06 to 11.06 MPa, following an exponential relationship.
(2) During the initial loading stage, stress increased linearly with strain. However, this linear relationship began to weaken after the strain exceeded 0.45%, marking the start of internal bond breakage accumulation. As axial strain continued to increase, the stress-strain curve progressively deviated further from its initial linear trajectory. The UCS was reached at an axial strain of 0.625%, by which time the internal shear bonding force chains had primarily aligned in a vertical orientation.
(3) The bond breakage and overall deformation of the rock were controlled primarily by the microscopic shear bonding force. The rock mass failed brittlely when the internal damage nucleated rapidly to form an interconnected failure plane. The ultimate failure of the rock distinctly presented a shear failure mode, characterized by a failure plane inclined at an approximate angle of 60°.

This research investigated into the microscopic mechanical behaviors of bonded particles, providing new insights into the nature of brittle failure in rock masses. It enhances the comprehension of the interplay between rock strength and internal damage, revealing crucial aspects of their co-variation and implications for structural integrity.

CRediT authorship contribution statement

Tao Zhao: Writing – original draft, Visualization, Validation, Software, Methodology, Investigation, Funding acquisition, Formal analysis, Data curation, Conceptualization. **Philip E.F. Collins:** Writing – review & editing, Supervision, Resources, Conceptualization.

Declaration of competing interest

The authors declare that they have no known competing financial interests or personal relationships that could have appeared to influence the work reported in this paper.

Acknowledgements

This research was supported by the UK Engineering and Physical Sciences Research Council (EPSRC) New Investigator Award (Grant No. EP/V028723/1) and the Royal Society, Sino-British Fellowship Trust International Exchanges Award (No. IES\R2\202023).

 The research data are publicly available online at: https://doi.org/10.17633/rd.brunel.25117811.

Appendix A. Unit quaternion and spatial rotation

According to Hamilton (1844), the unit quaternion is a quaternion with a unit length. It can be expressed as,

$$\boldsymbol{q} = q_0 + q_x\boldsymbol{i} + q_y\boldsymbol{j} + q_z\boldsymbol{k} \tag{A.1}$$

where $\boldsymbol{i}, \boldsymbol{j}, \boldsymbol{k}$ are the fundamental quaternion units (i.e. basis elements) and can be interpreted as unit-vectors pointing along the three Cartesian spatial axes. They have the properties as, $\boldsymbol{i}^2 = \boldsymbol{j}^2 = \boldsymbol{k}^2 = \boldsymbol{ijk} = -1$, $\boldsymbol{ij} = -\boldsymbol{ji} = \boldsymbol{k}, \boldsymbol{jk} = -\boldsymbol{kj} = \boldsymbol{i}$ and $\boldsymbol{ki} = -\boldsymbol{ik} = \boldsymbol{j}$.

The conjugate, norm and reciprocal of a unit quaternion $\boldsymbol{q}$ are defined as,

$$\boldsymbol{q}^* = q_0 - q_x\boldsymbol{i} - q_y\boldsymbol{j} - q_z\boldsymbol{k} \tag{A.2}$$

$$\|\boldsymbol{q}\| = \sqrt{\boldsymbol{q}\boldsymbol{q}^*} = \sqrt{q_0^2 + q_x^2 + q_y^2 + q_z^2} = 1 \tag{A.3}$$

$$\boldsymbol{q}^{-1} = \frac{\boldsymbol{q}^*}{\|\boldsymbol{q}\|^2} = \boldsymbol{q}^* \tag{A.4}$$

The rotation of a rigid object counterclockwise (view in the same direction as the axis vector) about a unit axis vector $\boldsymbol{u}$ by an angle of θ can be rewritten as a unit quaternion,

$$\boldsymbol{q} = \langle \cos\frac{\theta}{2}, \sin\frac{\theta}{2}\boldsymbol{u} \rangle \tag{A.5}$$

The multiplication of any two quaternions of generic forms $\boldsymbol{q}_1 = \langle a, \boldsymbol{u} \rangle$ and $\boldsymbol{q}_2 = \langle b, \boldsymbol{v} \rangle$ can be evaluated as,

$$\boldsymbol{q}_1\boldsymbol{q}_2 = (ab - \boldsymbol{u}\cdot\boldsymbol{v}) + (a\boldsymbol{v} + b\boldsymbol{u} + \boldsymbol{u}\times\boldsymbol{v}) \tag{A.6}$$

A quaternion can also represent a vector by setting the scaler part to 0, e.g. $\boldsymbol{u} = \langle 0, \boldsymbol{u} \rangle$. In the following sections, quaternions relating to spatial rotational operations are defined as units, and vectors are represented in quaternion forms, unless specified otherwise. For a vector $\boldsymbol{a} = (a_x, a_y, a_z)$, its rotation by a quaternion $\boldsymbol{q} = \langle \cos\frac{\theta}{2}, \sin\frac{\theta}{2}\boldsymbol{u} \rangle$ (i.e. rotation over the unit axis vector $\boldsymbol{u}$ by an angle of θ) can be evaluated by quaternion conjugation of $\boldsymbol{a}$ by $\boldsymbol{q}$ as,

$$\boldsymbol{a}' = \boldsymbol{q}\boldsymbol{a}\boldsymbol{q}^{-1} \tag{A.7}$$

For successive finite rotations of $\boldsymbol{a}$ by unit quaternions $\boldsymbol{q_1}$, $\boldsymbol{q_2}$, …, $\boldsymbol{q_n}$, the resultant quaternion $\boldsymbol{a}'$ can be expressed as,

$$\boldsymbol{a}' = (\boldsymbol{q}_n \ldots \boldsymbol{q}_2\boldsymbol{q}_1)\boldsymbol{a}\left(\boldsymbol{q}_1^{-1}\boldsymbol{q}_2^{-1}\ldots\boldsymbol{q}_n^{-1}\right) \tag{A.8}$$

In numerical analyses, the unit quaternion of a single particle is a function of time, $\boldsymbol{q}$(t), which describes how particle orientation varies relative to a fixed coordinate frame. Let $\boldsymbol{\omega}$**(t)** be the angular velocity of the particle evaluated in the same fixed coordinate frame. The derivative of $\boldsymbol{q}$(t) can be calculated as,

$$\dot{\boldsymbol{q}}(t) = \frac{1}{2}\boldsymbol{\omega}\boldsymbol{q}(t) \tag{A.9}$$

To solve this differential equation, the forward Euler method of a first-order accuracy can be used as,

$$\boldsymbol{q}(t+\Delta t) = \boldsymbol{q}(t) + \Delta t\dot{\boldsymbol{q}} + O\left(\Delta t^2\right) \tag{A.10}$$

or

$$\boldsymbol{q}(t+\Delta t) = \boldsymbol{q}(t) + \frac{1}{2}\Delta t\boldsymbol{\omega}\boldsymbol{q}(t) + O\left(\Delta t^2\right) \tag{A.11}$$

References

Alassi, H.T., Holt, R., 2012. Relating discrete element method parameters to rock properties using classical and micropolar elasticity theories. Int. J. Numer. Anal. Methods GeoMech. 36 (10), 1350–1367. https://doi.org/10.1002/nag.1056.

Barton, N., Shen, B., 2017. Risk of shear failure and extensional failure around over-stressed excavations in brittle rock. J. Rock Mech. Geotech. Eng. 9 (2), 210–225. https://doi.org/10.1016/j.jrmge.2016.11.004.

Carlà, T., Farina, P., Intrieri, E., Botsialas, K., Casagli, N., 2017. On the monitoring and early-warning of brittle slope failures in hard rock masses: examples from an open-pit mine. Eng. Geol. 228, 71–81. https://doi.org/10.1016/j.enggeo.2017.08.007.

Crosta, G.B., Frattini, P., Fusi, N., 2007. Fragmentation in the val pola rock avalanche, Italian Alps. J. Geophys. Res.: Earth Surf. 112. https://doi.org/10.1029/2005JF000455.

de Bono, J., McDowell, G., Wanatowski, D., 2015. Investigating the micro mechanics of cemented sand using DEM. Int. J. Numer. Anal. Methods GeoMech. 39 (6), 655–675. https://doi.org/10.1002/nag.2340.

Duan, K., Kwok, C.Y., 2016. Evolution of stress-induced borehole breakout in inherently anisotropic rock: insights from discrete element modeling. J. Geophys. Res. Solid Earth 121 (4), 2361–2381. https://doi.org/10.1002/2015JB012676.

Grady, D.E., 1981. Fragmentation of solids under impulsive stress loading. J. Geophys. Res. Solid Earth 86, 1047–1054. https://doi.org/10.1029/JB086iB02p01047.

Graells Rovira, A., Mirats Tur, J.M., 2009. Control and simulation of a tensegrity-based mobile robot. Robot. Autonom. Syst. 57 (5), 526–535. https://doi.org/10.1016/j.robot.2008.10.010.

Hajiabdolmajid, V., Kaiser, P.K., Martin, C.D., 2002. Modelling brittle failure of rock. Int. J. Rock Mech. Min. Sci. 39 (6), 731–741. https://doi.org/10.1016/S1365-1609(02)00051-5.

Hamilton, W.R., 1844. On quaternions; or on a new system of imaginaries in algebra. London, Edinburgh Dublin Phil. Mag. J. Sci. 25 (163), 10–13.

Jiang, M.J., Yu, H.-., Harris, D., 2005. A novel discrete model for granular material incorporating rolling resistance. Comput. Geotech. 32 (5), 340–357. https://doi.org/10.1016/j.compgeo.2005.05.001.

Keneti, A., Sainsbury, B., 2018. Review of published rockburst events and their contributing factors. Eng. Geol. 246, 361–373. https://doi.org/10.1016/j.enggeo.2018.10.005.

Ling, S., Li, Y., Yang, B., Jia, Z., 2022. Joint diagonalization for a pair of Hermitian quaternion matrices and applications to color face recognition. Signal Process. 198, 108560. https://doi.org/10.1016/j.sigpro.2022.108560.

Liu, X., Dai, F., Zhang, R., Liu, J., 2015. Static and dynamic uniaxial compression tests on coal rock considering the bedding directivity. Environ. Earth Sci. 73 (10), 5933–5949. https://doi.org/10.1007/s12665-015-4106-3.

Lv, Z., Zhao, Y., Feng, Z., 2022. Catastrophic failure mechanism of rock masses system and earthquake prediction based on percolation theory. Rock Mechanics Bulletin 1 (1), 100009. https://doi.org/10.1016/j.rockmb.2022.100009.

Ma, X., Dong, W., Hu, D., Zhou, H., 2023. Mechanical properties of granite at high temperature subjected to true triaxial compression. Int. J. Rock Mech. Min. Sci. 164, 105313. https://doi.org/10.1016/j.ijrmms.2022.105313.

Malachi Ozoji, T., Zhang, Z., Emman Aladejare, A., Zhang, N., Paasovaara, N., Rodriguez Arrieta, M., 2024. Effect of strain rate on specific fracture energy and micro-fracture surface properties of rock specimen under dynamic uniaxial compression. Eng. Fract. Mech. 295, 109763. https://doi.org/10.1016/j.engfracmech.2023.109763.

Manso, J., Marcelino, J., Caldeira, L., 2018. Crushing and oedometer compression of rockfill using DEM. Comput. Geotech. 101, 11–22. https://doi.org/10.1016/j.compgeo.2018.04.009.

Modenese, C., 2013. Numerical Study of the Mechanical Properties of Lunar Soil by the Discrete Element Method (DPhil).

Nova, R., Castellanza, R., Tamagnini, C., 2003. A constitutive model for bonded geomaterials subject to mechanical and/or chemical degradation. Int. J. Numer. Anal. Methods GeoMech. 27 (9), 705–732. https://doi.org/10.1002/nag.294.

Obermayr, M., Dressler, K., Vrettos, C., Eberhard, P., 2013. A bonded-particle model for cemented sand. Comput. Geotech. 49, 299–313. https://doi.org/10.1016/j.compgeo.2012.09.001.

Ohnaka, M., 2013. The Physics of Rock Failure and Earthquakes. Cambridge University Press, Cambridge. Retrieved from. https://www.cambridge.org/core/product/8C6A472930E8C414EABF1EF0E99CC41A.

Potyondy, D.O., Cundall, P.A., 2004. A bonded-particle model for rock. Int. J. Rock Mech. Min. Sci. 41 (8), 1329–1364. https://doi.org/10.1016/j.ijrmms.2004.09.011.

Rait, K.L., Bowman, E.T., Lambert, C., 2012. Dynamic fragmentation of rock clasts under normal compression in sturzstrom. Géotech. Lett. 2 (3), 167–172. https://doi.org/10.1680/geolett.12.00038.

Seelen, L.J.H., Padding, J.T., Kuipers, J.A.M., 2016. Improved quaternion-based integration scheme for rigid body motion. Acta Mech. 227 (12), 3381–3389. https://doi.org/10.1007/s00707-016-1670-x.

Shen, W., Zhao, T., Crosta, G.B., Dai, F., 2017. Analysis of impact-induced rock fragmentation using a discrete element approach. Int. J. Rock Mech. Min. Sci. 98, 33–38. https://doi.org/10.1016/j.ijrmms.2017.07.014.

Shen, Z., Jiang, M., Thornton, C., 2016. DEM simulation of bonded granular material. Part I: contact model and application to cemented sand. Comput. Geotech. 75, 192–209. https://doi.org/10.1016/j.compgeo.2016.02.007.

Sun, J., Frattini, P., Wang, X., De Blasio, F.V., Lanfranconi, C., Jiao, Q., Crosta, G.B., 2023. Deposit comminution in a weak variably-cemented breccia rock avalanche. Eng. Geol. 326, 107331. https://doi.org/10.1016/j.enggeo.2023.107331.

Thornton, C., Ciomocos, M.T., Adams, M.J., 1999. Numerical simulations of agglomerate impact breakage. Powder Technol. 105 (1), 74–82. https://doi.org/10.1016/S0032-5910(99)00120-5.

Utili, S., Zhao, T., Houlsby, G.T., 2015. 3D DEM investigation of granular column collapse: evaluation of debris motion and its destructive power. Eng. Geol. 186, 3–16. https://doi.org/10.1016/j.enggeo.2014.08.018.

Walmsley, S.H., 1988. A comparison of infinitesimal rotation, Quaternion and direction cosine coordinates in the dynamics of molecular clusters. J. Mol. Struct. 189 (1), 129–135. https://doi.org/10.1016/0022-2860(88)80219-9.

Wang, J., Liang, H., Sun, Z., Wu, S., Zhang, S., 2013. Relative motion coupled control based on dual quaternion. Aero. Sci. Technol. 25 (1), 102–113. https://doi.org/10.1016/j.ast.2011.12.013.

Wang, X., Cai, M., 2018. Modeling of brittle rock failure considering inter- and intra-grain contact failures. Comput. Geotech. 101, 224–244. https://doi.org/10.1016/j.compgeo.2018.04.016.

Wang, Y., 2009. A new algorithm to model the dynamics of 3-D bonded rigid bodies with rotations. Acta Geotechnica 4 (2), 117–127. https://doi.org/10.1007/s11440-008-0072-1.

Weatherley, Hancock, W., Boros, V., Abe, S., 2021. ESyS-Particle Tutorial and Users Guide. Retrieved from, Version 2.3.5. https://launchpad.net/esys-particle.

Xu, J., Li, H., Wang, H., Tang, L., 2023. Experimental study on 3D internal penny-shaped crack propagation in brittle materials under uniaxial compression. Deep Underground Science and Engineering 2 (1), 37–51. https://doi.org/10.1002/dug2.12037.

Xu, T., Tang, C.A., Yang, T.H., Zhu, W.C., Liu, J., 2006. Numerical investigation of coal and gas outbursts in underground collieries. Int. J. Rock Mech. Min. Sci. 43 (6), 905–919. https://doi.org/10.1016/j.ijrmms.2006.01.001.

Xu, T., Fu, T., Heap, M.J., Meredith, P.G., Mitchell, T.M., Baud, P., 2020. Mesoscopic damage and fracturing of heterogeneous brittle rocks based on three-dimensional polycrystalline discrete element method. Rock Mech. Rock Eng. 53 (12), 5389–5409. https://doi.org/10.1007/s00603-020-02223-y.

Yesiloglu-Gultekin, N., Gokceoglu, C., Sezer, E.A., 2013. Prediction of uniaxial compressive strength of granitic rocks by various nonlinear tools and comparison of their performances. Int. J. Rock Mech. Min. Sci. 62, 113–122. https://doi.org/10.1016/j.ijrmms.2013.05.005.

Zhang, L., Zhang, S., Yang, H., Cai, H., Qian, S., 2015. Relative attitude and position estimation for a tumbling spacecraft. Aero. Sci. Technol. 42, 97–105. https://doi.org/10.1016/j.ast.2014.12.025.

Zhang, Q.B., Zhao, J., 2014. A review of dynamic experimental techniques and mechanical behaviour of rock materials. Rock Mech. Rock Eng. 47 (4), 1411–1478. https://doi.org/10.1007/s00603-013-0463-y.

Zhao, T., Crosta, G.B., 2018. On the dynamic fragmentation and lubrication of Coseismic landslides. J. Geophys. Res. Solid Earth 123 (11), 9914–9932. https://doi.org/10.1029/2018JB016378.

Zhao, T., Crosta, G.B., Dattola, G., Utili, S., 2018. Dynamic fragmentation of jointed rock blocks during rockslide-avalanches: insights from discrete element analyses. J. Geophys. Res. Solid Earth 123 (4), 3250–3269. https://doi.org/10.1002/2017JB015210.

Zhao, T., Crosta, G.B., Utili, S., De Blasio, F.V., 2017. Investigation of rock fragmentation during rockfalls and rock avalanches via 3-D discrete element analyses. J. Geophys. Res.: Earth Surf. 122 (3), 678–695. https://doi.org/10.1002/2016JF004060.

Zou, C., Li, H., 2021. Combined numerical and experimental studies on the dynamic and quasi-static failure modes of brittle rock. Int. J. Rock Mech. Min. Sci. 148, 104957. https://doi.org/10.1016/j.ijrmms.2021.104957.